Approach Modeling and Control of an Autonomous Maneuverable Space Net

Meng, Zhongjie; Huang, Panfeng; Guo, Jian

Important note
To cite this publication, please use the final published version (if applicable).
Please check the document version above.

Approach Modeling and Control of an Autonomous Maneuverable Space Net

ZHONGJIE MENG (ID), Member, IEEE
PANFENG HUANG, Member, IEEE
Northwestern Polytechnical University, Xi'an China

JIAN GUO
Delft University of Technology, Delft, The Netherlands

The autonomous maneuverable space net, which consists of a flexible net and several maneuverable units, is a promising solution for the active removal of space debris. A novel dynamics model and a corresponding controller are proposed in this paper to resolve the approach control problem. Given that the net tethers cannot be elongated, interval functions and corresponding constraint forces are exploited to model the unilaterally constrained tethers. The proposed approach dynamics model, which is based on the Hamilton principle, includes distinctive velocity jump phenomena. A dual-loop control scheme with double optimization pseudo-dynamics inversion and sliding mode control is also established. Simulation results validate the feasibility of the proposed control scheme. The net can fly along the expected trajectory without suffering unexpected net deformation or orbital radial movement.

I. INTRODUCTION

Space debris is a problem that has continually increased in severity ever since Sputnik was launched on October 4, 1957; the growing orbital debris population has yet to be effectively controlled. Without effective debris mitigation solutions in the immediate future, the earth orbit will be too dangerous to launch new man-made spacecraft [1], [2]. Noncooperative target capture technology has attracted a great deal of research attention in recent years [3]–[5]. Previous studies [6], [7] have shown that the most effective way to capture noncooperative space debris is through the use of various types of space robots. Conventional rigid space robots such as the ETS VII, Canadarm, and Orbital Express [6], [8] can be used to capture cooperative targets, but it is difficult and dangerous for rigid space robots to capture noncooperative targets (i.e., targets with unknown basic parameters and structures).

The autonomous maneuverable space net (AMSN), which consists of several maneuverable units (MUs) and a flexible net, is a promising solution for noncooperative target capture. Compared to rigid space robots, the large net converts the point-to-point capture to a surface-to-point capture, which has several advantages in regards to noncooperative targets. First, AMSN can be applied to capture targets with different sizes and states. Second, the large net significantly reduces the requirements for control accuracy during the approach process. Compared to the tether net system (TNS) [9], the capture distance of the AMSN is much longer and the operation is more flexible due to the MUs. The typical structure and operational concept of the AMSN are shown in Figs. 1 and 2.

In the orbit launch phase, the AMSN is fixed to a platform which approaches the target from several hundred meters and releases the AMSN at a certain initial velocity. In the subsequent approach phase, the AMSN maintains its shape and flies toward the target under the control of thrusts on the MUs. Once the target enters the net mouth, the tethers (among concomitant MUs) are retrieved by electric motors and the net mouth closes. The target is captured by the AMSN and dragged to a graveyard orbit or into the atmosphere where it incinerates. In the approach phase, MU thrust is controlled in order to steer the deployed net toward the target. The net trajectory and shape are crucial for successful target capture.

The net is comprised of interwoven tethers, which come with limitations on dynamics and control, especially in the approach phase. The dynamics and control of a single tether are already a difficult problem, in fact, and one which many previous researchers have explored in regards to the tethered satellite system (TSS). Kane and Levinson [10], for example, completed fundamental research on TSS dynamics. Beletsky and Levin [11] investigated tether dynamics in the Newtonian field including stability and oscillatory behavior. Mankala and Agrawal [12] explored dynamics modeling using Newton's laws and Hamilton's principle. Krupa *et al.* [13] proposed a dynamics model and studied control techniques for tether deployment and retrieval;
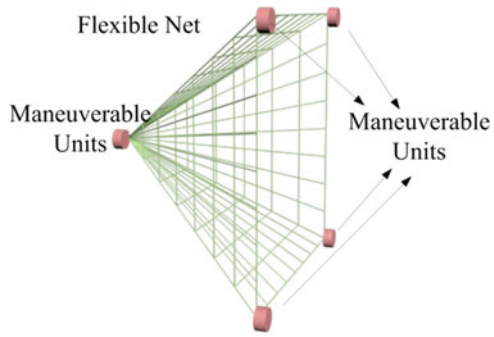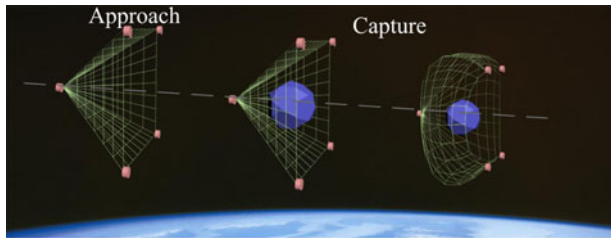
Fig. 1. Autonomous maneuverable space net (AMSN).

Fig. 2. Operational concept of the AMSN.

Fig. 3. Reference frames.

Misra [14] studied tether dynamics and control schemes to stabilize the tether retrieval; Williams [15] also studied control schemes for tether deployment and retrieval. Fujii *et al*. [16] studied the dynamics of a flexible space tether equipped with a crawler mass and Aslanov *et al*. [17] studied the dynamics at work after tether rupture. Tang *et al*. [18] studied the dynamics of variable-length tethers during deployment. Other works on the TSS are discussed at length in review articles by Kumar [19] and Cartmell and McKenzie [20]. In the space net field, the TNS is the most popular research object. Mankala and Agrawal [21], for example, investigated the deployment and retrieval of nets. Liu *et al*. [22] studied the deorbiting dynamics of the TNS. Zhai *et al*. [23], [24] developed dynamics equations for TNS in the orbital frame and studied the relationship between capture error and initial capture conditions. It is impossible to suppress the vibration using tension only due to the instability of in-plane vibration; and then a feed-forward controller equipped with thrusters is used to account for this.

All of the researchers mentioned above assume a large and flexible net to be a mass point while neglecting variations in the shape of the net. In a series of studies on net dynamics, Gärdsback and Tibert [25], [26] developed a dynamics model of the spinning space net and studied its optimal deployment control; the spinning net is modeled simply as a hub with several straight arms. Liu et al. [27] studied the orbit dynamics of the tethered combination system after net capture, where the net is modeled as four flexible bridles. These models are too simple to reflect the net dynamics in the approach phase. Zhang and Huang [28], [29] proposed a net dynamics model using Clohessy–Wiltshire equations and Hooke's law. Because the Young's modulus of the tether is more than 130 GPa, the vibration frequency
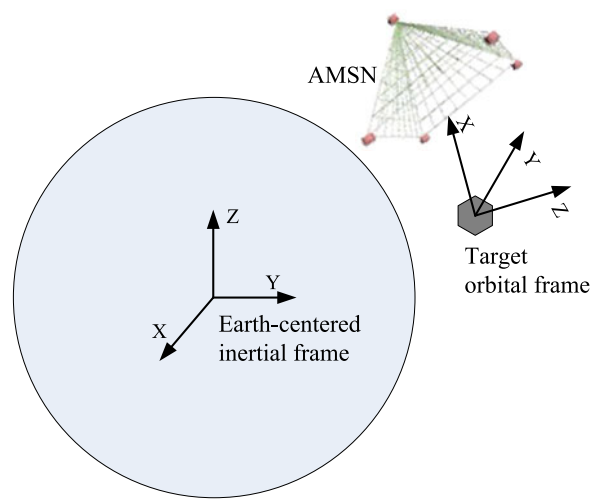
along the tether direction is very high. Thus, the simulation step must be extremely small to ensure the model remains stable throughout its solution; this is computationally burdensome and time-consuming. In a study by Huang *et al*. [29], the influences of connected tethers are ignored during the approach phase while MUs are controlled as separate mass points. This requires large thrusts and cannot achieve desired effects under actuator saturation. In an effort to resolve these problems, we developed a novel net description and dynamics model for the approach phase; a dual-loop flight control scheme is also proposed here under which the net holds its shape as it approaches the target.

This paper is organized as follows: Section II proposed a novel dynamics model with interval functions and corresponding constraint forces. Section III describes the flight controller in the target approach phase, which works via pseudo-dynamic inversion and sliding mode control. Section IV describes the simulations we ran to verify the feasibility and effectiveness of the proposed scheme. Conclusions are made finally in Section V.

II. AMSN DYNAMICS MODEL WITH UNILATERAL CONSTRAINTS

As shown in Fig. 3, two reference frames are defined in the dynamics modeling. The Earth-centered inertial frame (ECIF) is a nonrotating frame with its origin located at the mass center of the earth; its *x*-axis and *z*-axis are aligned with the equinox and spin axis of the earth, respectively. The target orbital frame (TOF) is formed with its origin in the mass center of the target. The *z*-axis is directed from the center of Earth to the mass center of the target and represents the system local vertical, the *y*-axis is the orbital angular momentum unit vector, and the *x*-axis completes the frame following the right-hand principle.

Modeling assumption A: For simplicity, the target is assumed to be in flight along a circular Keplerian orbit in this paper. The orbital angular velocity is ω.
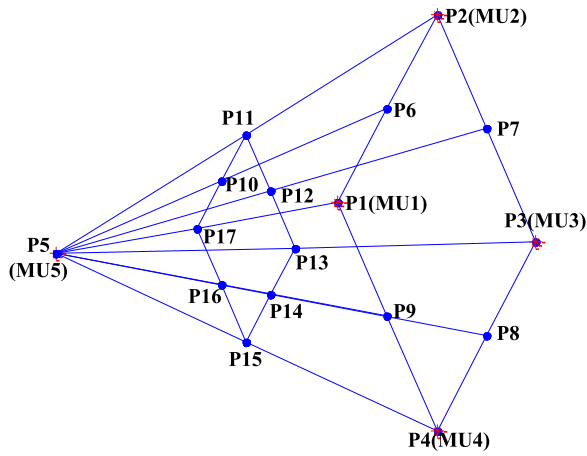
Fig. 4. AMSN structure.

A. Description of the AMSN

The AMSN is comprised of a huge net and several small MUs. The net can be up to hundreds of meters in size, while the MU is less than 0.5 m in size.

Modeling assumption B: Since the sizes of MUs are much smaller than the flexible net, the volumes of MUs are ignored in this paper; they instead are simplified as controllable mass points.

The structure of AMSN is similar to an isolated net, which is quite different from the TSS or TNS. Then, its structure can be represented by an undirected graph.

$$G = (V_n, E_c) \qquad (1)$$

where V_n is the nonempty vertex set and E_c is the edge set. The vertices include all the tether knit points; n is the number of vertices. The edges describe the connections of all the vertices; the number of edges is c. In the dynamics model, the adjacency matrix represents the undirected graph. In the adjacency matrix, the element 1 is replaced by the undeformed length of each edge.

The structure and dimensions of a representative system are shown in Fig. 4. The system contains 17 tether knit points and five MUs. Then, n is 17 and c is 32.

B. Tether Dynamics Model

In [30], Buckham studied the application of low tension tethers and verified that the lumped-mass dynamics model is suitable for low-tension tether simulation. In the approach phase, the tether tension in the net is generally small.

Modeling assumption C: The lumped-mass method is used here to concentrate tether mass at the knit points (while torsion is ignored).

The extant literature suggests that two models are applicable here: The rigid rod model [31], [32], in which the elasticity and flexibility of tether are ignored, and the bead model [14]–[16], in which the tether tension–strain relation is

$$N = \begin{cases} EA\,(\varepsilon + \alpha\dot{\varepsilon}) & \varepsilon \geq 0 \\ 0 & \varepsilon < 0 \end{cases} \qquad (2)$$

where N is the tether tension, ε is the tether strain, α is the damping coefficient, A is the sectional area of the tether, and E is the Young's modulus.

The bead model is higher fidelity in contrast to the rigid rod model. However, the tether is woven by Kevlar or other synthetic fibers with extremely high stiffness and its Young's modulus can reach or exceed 130 GPa. The vibration frequency along the tether direction is very high. Thus, the simulation step is extremely small to ensure stabilization as the bead model is solved. On the other hand, the movement of the AMSN is rather smooth and the tether tension is small in the approach phase. Then, the tether strain is so small that it can be neglected.

Modeling assumption D: In order to further simplify the dynamics model, it is assumed that EA is infinite. The tether cannot be elongated and the tether strain ε is zero, in other words.

Equation (2) cannot be used for the tether dynamics description. The interval function and corresponding constraint forces can be applied to this unilateral constraint problem [33], [34].

The interval function is

$$g_{ij} = L_{ij} - \left\| \boldsymbol{R}_i - \boldsymbol{R}_j \right\| \geq 0 \qquad (3)$$

where L_{ij} is the undeformed tether length between vertex i and vertex j, $\boldsymbol{R}_i$ and $\boldsymbol{R}_j$ are the positions of vertex i and vertex j in the ECIF, respectively.

The corresponding constraint force is

$$\lambda_{ij} \begin{cases} = 0 & \text{when } g_{ij} > 0 \cup g_{ij} = 0 \text{ and } \dot{g}_{ij} > 0 \\ = 0 & \text{when } g_{ij} = 0, \dot{g}_{ij} = 0 \text{ and } \ddot{g}_{ij} > 0 \\ \geq 0 & \text{when } g_{ij} = 0, \dot{g}_{ij} = 0 \text{ and } \ddot{g}_{ij} = 0 \end{cases} . \quad (4)$$

The constraint force is an approximate version of the tension along the corresponding tether. Generally, when dynamic equations are solved by numerical integration algorithms, the zero-order item g_{ij} and first-order item $\dot{g}_{ij}$ are known while the second-order item $\ddot{g}_{ij}$ is unknown. If the constraint belongs to the first case, the solution is obtained without the unilateral constraint. If it belongs to the latter two cases, $\ddot{g}_{ij}$ and λ_{ij} must be solved first. (This is discussed in detail below, where the overall dynamics equations are derived.)

The interval functions and corresponding constraint forces of the AMSN can be represented as vectors $\boldsymbol{g}_C$ and $\boldsymbol{\lambda}_C$. The dimensions of both vectors are c.

C. AMSN Dynamics Model

According to modeling assumptions B and C, the MUs and tether knit points in the net are modeled as mass points. The Lagrange function of the AMSN includes the kinetic energy and potential energy of all knit points and controllable mass points:

$$L = \sum_{i=1}^{n} m_i \left[\frac{1}{2} \boldsymbol{R}_i^{\mathrm{T}} \boldsymbol{R}_i - \frac{GM}{\|\boldsymbol{R}_i\|} \right] \qquad (5)$$

where G is the universal gravitational constant, M is the Earth's mass, m_i and $\boldsymbol{R}_i$ are the mass and position of point i in the ECIF, respectively. All the m_i values are kept constant by ignoring the propellant expenditures of MUs.

The virtual work of nonconventional forces acting on the AMSN is

$$\delta'W = \sum_{i=1}^{n} \delta \boldsymbol{R}_i^{\mathrm{T}} \boldsymbol{F}_i + \delta \boldsymbol{g}_C \boldsymbol{\lambda}_C \qquad (6)$$

where $\boldsymbol{F}_i$ is the thrust on the point i. The thrusters are configured on the MUs, so thrusts of the other points are zero.

According to the extended Hamilton's principle

$$\int_{t_0}^{t_1} \left(\delta L + \delta'W \right) \mathrm{d}t = 0 \qquad (7)$$

the dynamics model of the AMSN is

$$\int_{t_0}^{t_1} \left[\sum_{i=1}^{n} m_i \delta \left(\frac{1}{2} \boldsymbol{R}_i^{\mathrm{T}} \boldsymbol{R}_i - \frac{GM}{\|\boldsymbol{R}_i\|} \right) \right.$$
$$\left. + \sum_{i=1}^{n} \delta \boldsymbol{R}_i^{\mathrm{T}} \boldsymbol{F}_i + \delta \boldsymbol{g}_C \boldsymbol{\lambda}_C \right] \mathrm{d}t = 0. \qquad (8)$$

Equation (8) is difficult to simplify enough to reflect the AMSN orbit motion. Define the target position in the ECIF as $\boldsymbol{R}_0$ and the position of point i in the TOF as $\boldsymbol{r}_i$, then

$$\boldsymbol{R}_i = \boldsymbol{R}_0 + \boldsymbol{r}_i. \qquad (9)$$

Under modeling assumption A and the C-W equation, (8) is simplified to

$$M\ddot{\boldsymbol{r}}_N + C\dot{\boldsymbol{r}}_N + K\boldsymbol{r}_N = \boldsymbol{F} + \left(\frac{\partial \boldsymbol{g}_C}{\partial \boldsymbol{r}_N} \right)^{\mathrm{T}} \boldsymbol{\lambda}_C \qquad (10)$$

where

$$\begin{cases} M = \mathrm{diag}\,(m_1, m_2, \ldots, m_n) \otimes \mathrm{diag}\,(1, 1, 1) \\ C = \mathrm{diag}\,(m_1, m_2, \ldots, m_n) \otimes M_{\dot{r}} \\ K = \mathrm{diag}\,(m_1, m_2, \ldots, m_n) \otimes M_r \\ \boldsymbol{r}_N = \left[\boldsymbol{r}_1^{\mathrm{T}}, \boldsymbol{r}_2^{\mathrm{T}}, \ldots, \boldsymbol{r}_i^{\mathrm{T}}, \ldots \boldsymbol{r}_n^{\mathrm{T}} \right]^{\mathrm{T}} \\ \boldsymbol{F} = \left[\boldsymbol{F}_1^{\mathrm{T}}, \boldsymbol{F}_2^{\mathrm{T}}, \ldots, \boldsymbol{F}_i^{\mathrm{T}}, \ldots, \boldsymbol{F}_n^{\mathrm{T}} \right]^{\mathrm{T}} \end{cases}$$

$$M_{\dot{r}} = \begin{bmatrix} 0 & 0 & -2\omega \\ 0 & 0 & 0 \\ 2\omega & 0 & 0 \end{bmatrix}, M_r = \begin{bmatrix} 0 & 0 & 0 \\ 0 & \omega^2 & 0 \\ 0 & 0 & -3\omega^2 \end{bmatrix}.$$

The unelongated tether also has distinct velocity jump dynamic phenomena. A relevant scenario is depicted in Fig. 5. At time t^-, the distance between point i and point j reaches the undeformed tether length L_{ij} while the relative velocity along the tether between the two points is not zero, and they have a tendency to move away from each other. The tether becomes taut at time t and the tightening force is transferred through the tether, which is similar to an impact process. Due to the high damping of the braided structure and the stiffness of the tether, at time t^+, the two points have the same velocity along the tether.
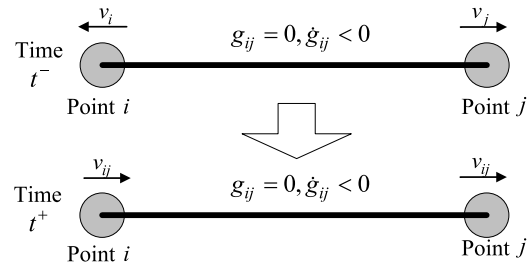

Fig. 5. Velocity jump scenarios.

Equation (10) can be integrated with the time interval $[t^-, t^+]$ and simplified as follows:

$$M \left(\dot{\boldsymbol{r}}_N|_{t^+} - \dot{\boldsymbol{r}}_N|_{t^-} \right) = \left(\frac{\partial \boldsymbol{g}_C}{\partial \boldsymbol{r}_N} \right)^{\mathrm{T}} \boldsymbol{\Lambda}_C \qquad (11)$$

where $\boldsymbol{\Lambda}_C$ is the integration of $\boldsymbol{\lambda}_C$ over $[t^-, t^+]$.

Given the interval function vector of tethers has the velocity jump $\boldsymbol{g}_{CT}$, then

$$\dot{\boldsymbol{g}}_{CT}\big|_{t^+} = \boldsymbol{0}. \qquad (12)$$

Solving (11) and (12) together yields the velocity vector at time t^+.

Compared to the bead model, the main difference in this model is that the tether is assumed to be unelongated and the velocity jump is used to describe the elongation trend. This is similar to the collision of two bodies, in which it is typically assumed that the bodies are rigid. The tensile strength of the space tether is extremely high. The Young's modulus of steel, copper, and aluminum is 200, 110, and 69 GPa, respectively. The Young's modulus of the tether, by contrast, is more than 130 GPa. Generally, the tether tension is less than 10 N. The actual elongation length is less than 0.08 mm, which is ignored here.

D. Numerical Treatment

In numerical treatment, the problem is to solve $\boldsymbol{\lambda}_C$. As shown in (4), if $g_{ij} = 0$ and $\dot{g}_{ij} = 0$, λ_{ij} should be calculated first. All the items in interval function vector $\boldsymbol{g}_C$, which satisfies $g_{ij} = 0$ and $\dot{g}_{ij} = 0$, are taken out and represented as $\bar{\boldsymbol{g}}_C$. The corresponding constraint force vector is $\bar{\boldsymbol{\lambda}}_C$. Constraint forces (except $\bar{\boldsymbol{\lambda}}_C$ in $\boldsymbol{\lambda}_C$) are zero:

$$\begin{cases} \boldsymbol{g}_C = \boldsymbol{M}_R \bar{\boldsymbol{g}}_C \\ \boldsymbol{\lambda}_C = \boldsymbol{M}_R \bar{\boldsymbol{\lambda}}_C \end{cases} \qquad (13)$$

where $\boldsymbol{M}_R$ is the transformation matrix, which is composed of 0 and 1.

The second derivative of $\bar{\boldsymbol{g}}_C$ is calculated as follows:

$$\ddot{\bar{\boldsymbol{g}}}_C = \frac{\partial \bar{\boldsymbol{g}}_C}{\partial \boldsymbol{r}_N} \ddot{\boldsymbol{r}}_N + \frac{\partial^2 \bar{\boldsymbol{g}}_C}{\partial \boldsymbol{r}_N^2} \dot{\boldsymbol{r}}_N \cdot \dot{\boldsymbol{r}}_N. \qquad (14)$$

Inserting (10) and (13) into (14) yields

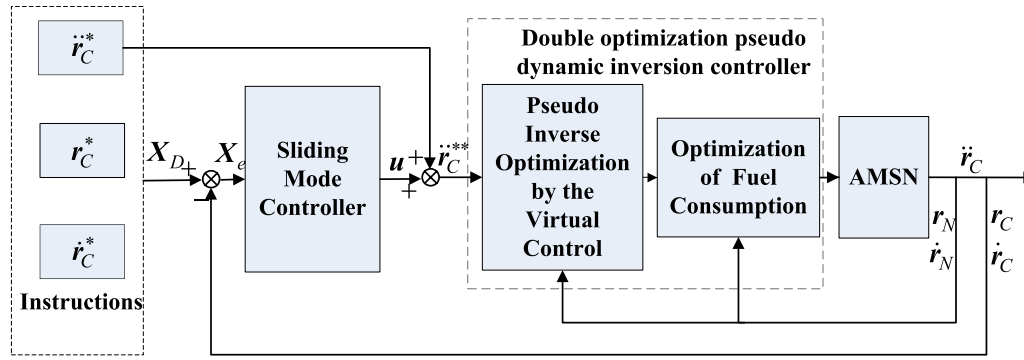$$\ddot{\bar{\boldsymbol{g}}}_C = A \bar{\boldsymbol{\lambda}}_C + B \qquad (15)$$

Fig. 6. Controller structure.

where

$$A = \frac{\partial \bar{g}_C}{\partial r_N} M^{-1} \left(\frac{\partial g_C}{\partial r_N} \right)^{\mathrm{T}} M_R$$

$$B = \frac{\partial \bar{g}_C}{\partial r_N} M^{-1} (F - C\dot{r}_N - K r_N) + \frac{\partial^2 \bar{g}_C}{\partial r_N^2} \dot{r}_N \cdot \dot{r}_N.$$

Considering the constraints conformed by $\bar{g}_C$, the constraint forces are solved as follows:

$$\begin{cases} \bar{g}_C = 0, \dot{\bar{g}}_C = 0 \\ \ddot{\bar{g}}_C = A\bar{\lambda}_C + B \\ \ddot{\bar{g}}_C^{\mathrm{T}} \bar{\lambda}_C = 0, \ddot{\bar{g}}_C \geq 0, \bar{\lambda}_C \geq 0 \end{cases} . \quad (16)$$

This is a typical linear complementarity problem. It can be solved using the Lemke algorithm [35].

With a time t and an integral step Δt, the step-wise model solution process of the AMSN is as follows:

1) At time t, the interval functions of all connecting tethers in E_c are calculated and $\bar{g}_C$ is separated.
2) The corresponding $\bar{\lambda}_C$ is calculated by solving (16).
3) $\ddot{r}_N$ is calculated by

$$\ddot{r}_N = M^{-1} \Big[F + \Big(\frac{\partial g_C}{\partial r_N} \Big)^{\mathrm{T}} \lambda_C - C\dot{r}_N - K r_N \Big].$$

4) The Runge Kutta method is used to calculate r_N and $\dot{r}_N$ of the time $(t + \Delta t)$.
5) The velocity jump is probed: If it exists, the actual velocity vector of time $(t + \Delta t)$ is calculated by solving (11) and (12).
6) Return to Step 1 and solve the dynamic states of the next integral time.

III. AMSN APPROACH CONTROL

The net shape, which is controlled by the MUs, is crucial in regards to target capture. The implicit λ_C with respect to r_N and $\dot{r}_N$ is a problematic aspect of controller design. Here, a dual-loop controller is designed with all measurable vertex states by referring to the contact control of rigid robots. The controller structure is shown in Fig. 6. The inner loop is a double optimization pseudo-dynamic inversion controller and the outer loop is a sliding mode controller. The positions, velocities, and accelerations of MUs are r_C,

$\dot{r}_C$, and $\ddot{r}_C$, respectively. The trajectory instructions are r_C^* and velocity instructions and acceleration instructions are $\dot{r}_C^*$ and $\ddot{r}_C^*$, respectively. F_C is the actual control vector consisting of MU thrusts. By the transformation matrix M_F, $F = M_F F_C$.

A. Pseudo-Dynamic Inversion Controller

The goal of the Moor–Penrose pseudo-inverse method is to search for a solution with minimal error. To this effect, an inverse dynamics problem can be transformed into an optimization problem. The goal of optimization is to solve the control force and the acceleration which conform to the dynamics constraints while minimizing the error between the actual and expected accelerations.

Due to interval functions and corresponding constraint forces, it is difficult to convert the dynamics inversion to a traditional optimization problem. A double optimization pseudo-dynamics inversion controller is proposed to resolve this problem.

First, the virtual control variable T converts the problem to the traditional dynamic inversion:

$$T = F + \left(\frac{\partial g_C}{\partial r_N} \right)^{\mathrm{T}} \lambda_C. \quad (17)$$

Then, the dynamic inversion problem is converted to an optimization problem:

$$\begin{cases} \min J = \frac{1}{2} \big(\ddot{r}_C - \ddot{r}_C^{**} \big)^{\mathrm{T}} \big(\ddot{r}_C - \ddot{r}_C^{**} \big) \\ \text{Constraint I: } M\ddot{r}_N + C\dot{r}_N + K r_N = T \\ \text{Constraint II: } \ddot{\bar{g}}_C \geq 0 \end{cases} \quad (18)$$

where $\bar{g}_C$ includes all interval functions with corresponding constraint forces that satisfy the last two cases described in (4).

Next, actual control variables are optimized by the virtual control variable T. The goal of this optimization is to ensure minimum fuel consumption:

$$\begin{cases} \min J = \frac{1}{2} F_C^{\mathrm{T}} F_C \\ \text{Constraint I: } M_F F_C + \left(\frac{\partial g_N}{\partial r_N} \right)^{\mathrm{T}} \lambda_N = T \\ \text{Constraint II: } \lambda_N \geq 0 \end{cases} . \quad (19)$$

The optimizations represented by (18) and (19) are both convex optimizations, so they can be readily solved mathematically. For example, the optimization problem can be transformed into a sequential quadratic programming problem and solved via an interior-reflective Newton method [36].

B. Sliding Mode Controller

An outer loop controller is necessary given the deviation between the pseudo-inverse model and actual inverse model. A sliding model controller is used here for this purpose. After the pseudo-inverse controller, the system dynamics model is written as follows:

$$\dot{X} = AX + Bu \tag{20}$$

where

$$X = \begin{bmatrix} r_C & \dot{r}_C \end{bmatrix}^T, \quad A = \begin{bmatrix} 0 & I \\ 0 & 0 \end{bmatrix}, \quad B = \begin{bmatrix} 0 & I \end{bmatrix}^T.$$

Given the control instruction X_D, the tracking error is $X_e = X_D - X$. The integral-type sliding mode surface is designed [37]

$$s = C \left[X_e - \int_0^t (A + BK) X_e dt \right] \tag{21}$$

where K is the state feedback gain matrix and C is a matrix composed of all positive numbers.

The sliding mode controller is

$$u = B^+(\dot{X}_D - AX_D) - K(X_D - X) + f \text{sgn}(s) \tag{22}$$

where B^+ is the Moore–Penrose pseudo-inverse of the matrix B and f is a positive coefficient.

The stability is expressed as follows:

$$\begin{aligned} s\dot{s} &= s[C(\dot{X}_D - \dot{X}) - C(A + BK)(X_D - X)] \\ &= s[C(\dot{X}_D - AX - Bu) - C(A + BK)(X_D - X)] \\ &= -CBfs \text{sgn}(s) \\ &= -CBf |s| \leq 0. \end{aligned}$$

Thus, the asymptotically stable system meets the sliding condition. Besides, the saturation function is used to replace the sign function for inhibiting the vibration of sliding surface:

$$\text{sat}(s_i, \varepsilon) = \begin{cases} 1 & s_i > \varepsilon \\ s_i/\varepsilon & -\varepsilon \leq s_i \leq \varepsilon \\ -1 & s_i < -\varepsilon \end{cases} \tag{23}$$

where ε is a small positive number.

IV. NUMERICAL EXAMPLES

The proposed control scheme and equations derived above are verified through a series of simulations. The structure and generalized coordinates are shown in Figs. 3 and 4. The orbital angle velocity of the target is 0.0011 rad/s, the line density of the tether is 4.5 g/m, and the mass of MU1–MU5 is 10 kg.
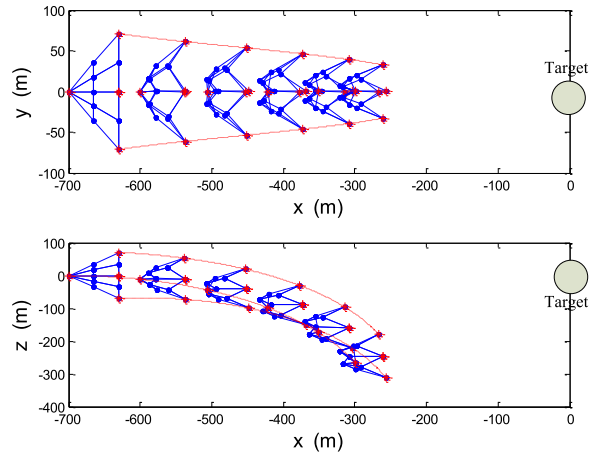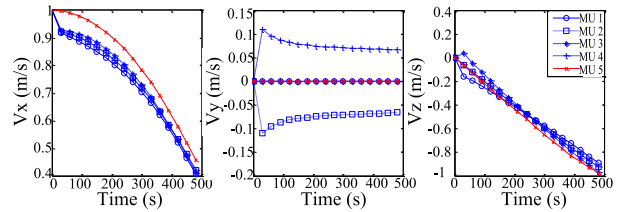

Fig. 7.   Approaching the target in Example 1.

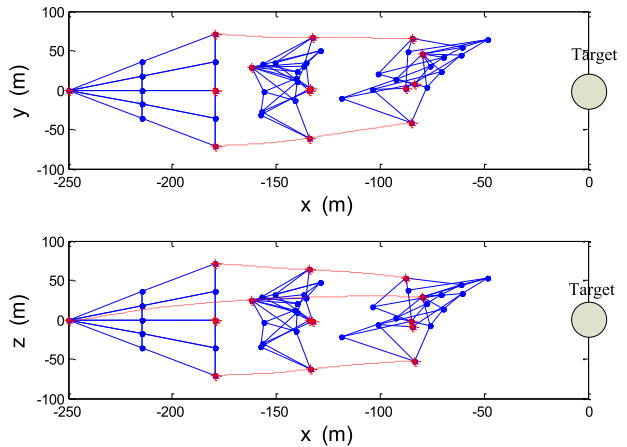Fig. 8.   Velocities of MUs in Example 1.

Fig. 9.   Approaching the target in Example 2.

A. Approaching the Target in a Noncontrolled Manner

EXAMPLE 1   The strains of the AMSN tethers are zero. The initial positions of MUs are

$$\begin{cases} r_1 = \begin{bmatrix} -700 + 50\sqrt{2} & 0 & 50\sqrt{2} \end{bmatrix}^T \text{m} \\ r_2 = \begin{bmatrix} -700 + 50\sqrt{2} & 50\sqrt{2} & 0 \end{bmatrix}^T \text{m} \\ r_3 = \begin{bmatrix} -700 + 50\sqrt{2} & 0 & -50\sqrt{2} \end{bmatrix}^T \text{m} \\ r_4 = \begin{bmatrix} -700 + 50\sqrt{2} & -50\sqrt{2} & 0 \end{bmatrix}^T \text{m} \\ r_5 = \begin{bmatrix} -700 & 0 & 0 \end{bmatrix}^T \text{m} \end{cases}.$$

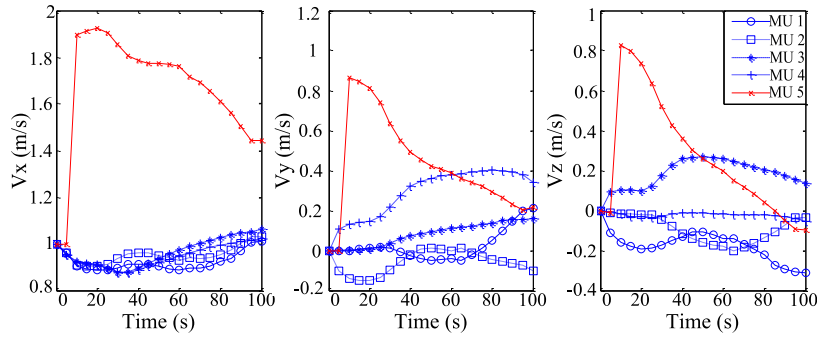The initial velocities of MUs in the TOF are $[1, 0, 0]^T$ m/s. Initial velocities of the other tether knit
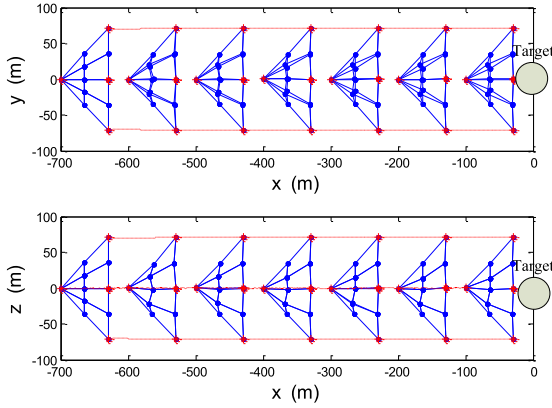
Fig. 10.   Velocities of MUs in Example 2.

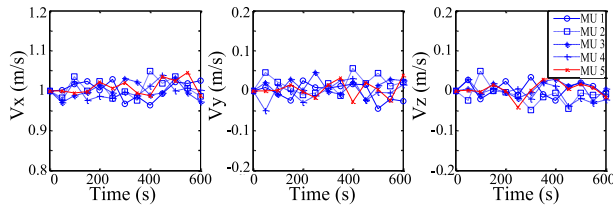Fig. 11.   Controlled motion in Example 3.
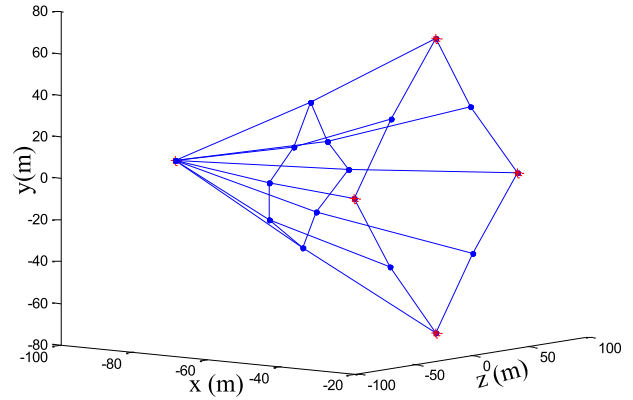

Fig. 13.   Terminal shape in Example 3.

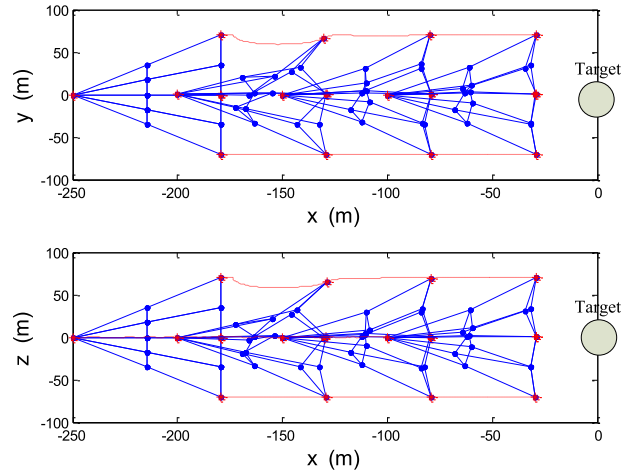Fig. 12.   Velocities of MUs in Example 3.

Fig. 14.   Controlled motion in Example 4.

points are $[0, 0, 0]^T$ m/s, and the position of target debris is $[0\ 0\ 0]^T$ m.

The target approach process without control is shown in Figs. 7 and 8. The AMSN approaches the target along the TOF x-axis, and during a 500 s flight, MUs 1–5 fly about 432.81, 439.61, 443.63, 439.71, and 400.61 m along the x-axis and about –250.09, –245.72, –240.59, –245.65, and –265.74 m along the z-axis. MU 2 and MU 4 fly about –37.94 and 37.97 m along the y-axis, respectively. The net shrinks in the x–y plane view. At 0, 250, and 500 s, the distances between MU 2 and MU 4 is about 141.42, 99.75, and 65.52 m. The areas of the net mouth are 5924.3 m^2 at 250 s and 4336.0 m^2 at 500 s. The surrounding knit points make an "M" shape at the net bottom.

The net falls rapidly in the x–z plane view at a rate which increases with flight time. The MU velocities are shown in Fig. 8. In MU 5, for example, the velocity changes from $[1, 0, 0]^T$ to $[0.4136, 0, -1.0075]^T$ m/s. The AMSN shrinks and falls due to the Coriolis force.

EXAMPLE 2   The strains of the AMSN tethers are zero. The initial positions of MUs are

$$
\begin{cases}
\boldsymbol{r}_1 = \begin{bmatrix} -250 + 50\sqrt{2} & 0 & 50\sqrt{2} \end{bmatrix}^T \text{m} \\
\boldsymbol{r}_2 = \begin{bmatrix} -250 + 50\sqrt{2} & 50\sqrt{2} & 0 \end{bmatrix}^T \text{m} \\
\boldsymbol{r}_3 = \begin{bmatrix} -250 + 50\sqrt{2} & 0 & -50\sqrt{2} \end{bmatrix}^T \text{m} \\
\boldsymbol{r}_4 = \begin{bmatrix} -250 + 50\sqrt{2} & -50\sqrt{2} & 0 \end{bmatrix}^T \text{m} \\
\boldsymbol{r}_5 = \begin{bmatrix} -250 & 0 & 0 \end{bmatrix}^T \text{m}
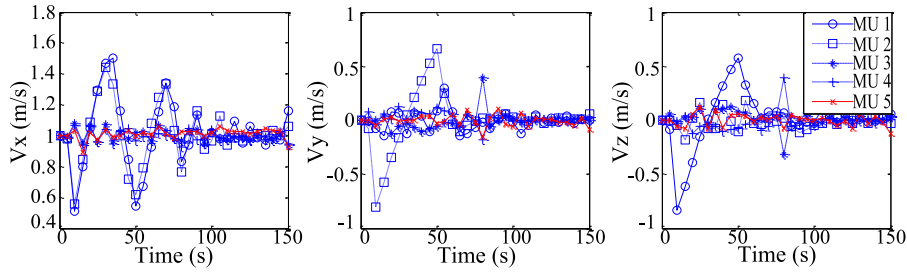\end{cases} .
$$

Fig. 15. Velocities of MUs in Example 4.

The initial velocities of MUs in TOF are $[1, 0, 0]^T$ m/s. Initial velocities of the other tether knit points are $[0, 0, 0]^T$ m/s and the position of the target debris is $[0\ 0\ 0]^T$ m. To simulate the impact of the net and the undesirable debris, an $[-10, -10, -10]^T$ Ns impulse is imposed on the tether knit point P10 at $t = 5$ s.

The target approach process without control is shown in Figs. 9 and 10. The velocity of P10 increases due to the impact of the debris while other tether knit points such as P5, P11, and P17 increase in velocity due to the tether tension. However, for the tether tensions are non-negative, some tether knit points (e.g., P1, P2, P3, and P4) cannot gain extra velocity. This is what forces the net into chaos and makes it fail to capture the target.

These examples demonstrate that the space net is sensitive to initial conditions and external disturbances. Trajectory control and shape maintenance methods are required to ensure successful target capture.

B. Approaching the Target Under the Controller

EXAMPLE 3 Due to the constrained MU thrusts, the actuator saturations in these examples are $[-0.3\ N, 0.3\ N]$. The initial states are the same as Example 1. Selecting controller parameters in this example as $\boldsymbol{K} = -0.03[\boldsymbol{I}_{15}, 5\boldsymbol{I}_{15}]$, $\boldsymbol{C} = \boldsymbol{1}_{15\times30}$, and $f = 0.1$. The ideal controlled motion is shown in Fig. 11. Under the controller, the AMSN approaches the target along the TOF x-axis. Motions along the y-axis and z-axis approximate to zero. Take MU 5 as an example, its position is changed from $[-1000, 0, 0]^T$ to $[-400.19, 0.13, -0.02]^T$ m while the net shape is effectively maintained. The distance between MUs 1 and 3 changes from 141.42 to 141.27 m while the distance between MUs 2 and 4 changes from 141.42 to 141.48 m. By contrast to 10 000 m^2 at 0 s, the area of the net mouth is about 9989.0 m^2 at 600 s.

The MU velocities are shown in Fig. 12. The maximum velocity change is still below 0.05 m/s, suggesting that the controller can effectively overcome Coriolis force. The net also exhibits only slight deformation even though the knit points are uncontrolled. The terminal shape of this simulation is shown in Fig. 13.

EXAMPLE 4 An extra impulse is added to simulate the impact of the net and the undesirable debris under the same initial states as Example 2. The controlled motion is shown
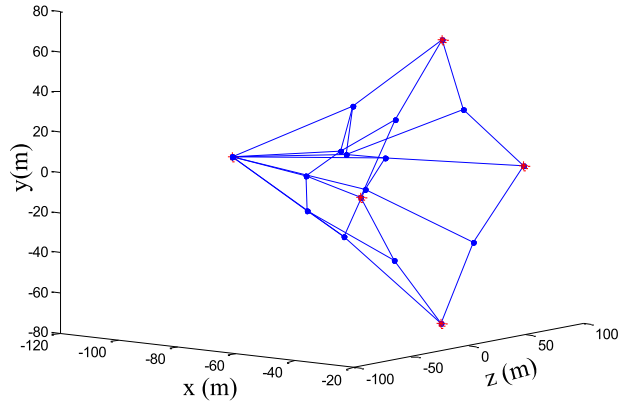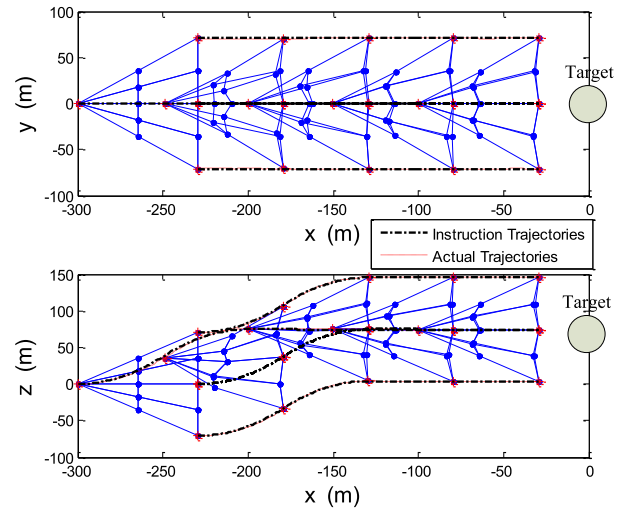

Fig. 16. Terminal shape in Example 4.

Fig. 17. Radial maneuver of AMSN.

in Fig. 14. The AMSN approaches the target along the x-axis in the TOF, while motions along the y-axis and z-axis approximate to zero. The net shape varies considerably due to the extra impulse but does regress to its initial shape under the controller, which validates the effectiveness of the controller.

The MU velocities in this example, as shown in Fig. 15, tend toward stabilization with maximal changes less than 0.8 m/s. The terminal shape, as shown in Fig. 16, is
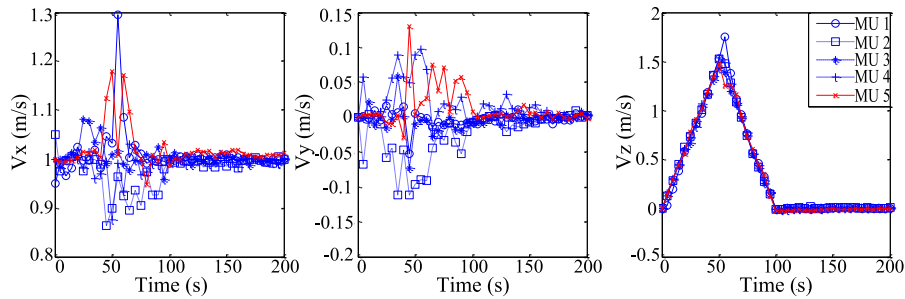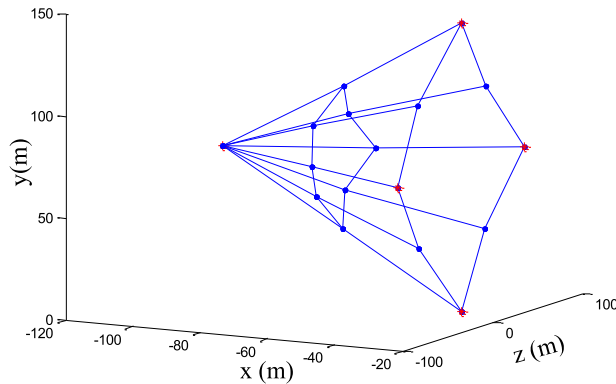
Fig. 18. MU maneuver velocities.

Fig. 19. Terminal shape in Example 5.

similar to the shape shown in Fig. 14. By contrast to 10 000 m² at 0 s, the area of the net mouth is about 9980.0 m² at 150 s. The net shape under the controller proposed by Huang in [27], by contrast, goes into chaos because the controller necessitates large thrust and the thrust is constrained in our example.

EXAMPLE 5 Due to the short flying time of the AMSN, orbit perturbations are very small. However, there are still other model errors necessary to consider, such as launch synchronization, measurement errors, and thrust errors. In this example, the initial velocities of MU1 and MU2 have −5% and 5% deviations, respectively. Measurement errors are random and the bound is assumed to be [−5 cm, 5 cm], which is much larger than the actual elongation length of the tether. The thrust errors of every MU are also random and the max deviation is 5%.

In addition, given the AMSN needs a radial maneuver in the approach phase, an ideal radial maneuvering trajectory is established first. Broken black lines in Figs. 17 and 18 indicate instruction trajectories and velocities. Simulations are then conducted to verify the controller's effectiveness. Under the controller, the AMSN performs the designed radial maneuver while the net maintains its shape. In other words, net deformation and orbital radial movement are suppressed by the controller. Fig. 19 shows the terminal shape, which is again similar to the shape shown in Fig. 13.

By contrast to 10 000 m² at 0 s, the area of the net mouth is about 9990.0 m² at 200 s.
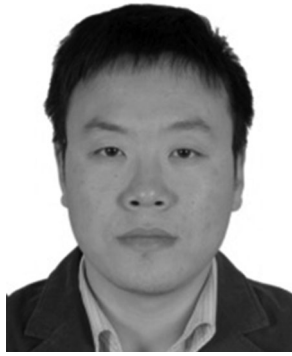
V. CONCLUSION

The necessity for removing undesirable space debris has made noncooperative target capture technology an increasingly popular research objective in recent years. Compared to rigid space robots, the AMSN converts the point-to-point capture to a surface-to-point capture, which is better suited to noncooperative capture. A novel dynamics model based on the Hamilton principle is derived above for the complex rigid-flexible coupling system. The AMSN is described as an undirected graph and adjacency matrix. Interval functions and corresponding constraint forces are used to model the unilateral constraint tethers, while the velocity jump model is obtained by integrating the dynamic equations over an infinitesimal period. A corresponding dual-loop control scheme is designed in which the inner loop is a double optimization pseudo-dynamic inversion controller and the outer loop is a traditional sliding mode controller. Simulation results indicated that the controller is effective in overcoming Coriolis force while preventing net deformation and orbital radial movements. Besides, the controller's robustness is also validated in the simulation. Under initial state errors, measurement errors, and thrust errors, the net can fly along the expected trajectory without losing its shape.

In the future study, the dynamics and control scheme in the actual capture of rotating space debris will be investigated.

REFERENCES

[1] E. Pate-Cornell and M. Sachon
    Risks of particle hits during space walks in low Earth orbit
    IEEE Trans. Aerosp. Electron. Syst., vol. 37, no. 1, pp. 134–146, Jan. 2001.
[2] J. Yu *et al.*
    Optimal scheduling of GEO debris removing based on hybrid optimal control theory
    Acta Astronaut., vol. 93, pp. 400–409, 2014.
[3] D. K. Wang, P. F. Huang, and Z. J. Meng
    Coordinated stabilization of tumbling targets using tethered space manipulators
    IEEE Trans. Aerosp. Electron. Syst., vol. 51, no. 3, pp. 2420–2432, Jul. 2015.

[4] P. F. Huang *et al.*
Adaptive postcapture backstepping control for tumbling tethered space robot-target combination
J. Guid. Control Dyn., vol. 39, no. 1, pp. 150–156, 2016.

[5] P. F. Huang, D. K. Wang, Z. J. Meng, F. Zhang, and Z. Liu
Impact dynamic modelling and adaptive target capturing control for tethered space robots with uncertainties
IEEE/ASME Trans. Mechatron., vol. 21, no. 5, pp. 2260–2271, Oct. 2016.

[6] M. Shan, J. Guo, and E. Gill
Review and comparison of active space debris capturing and removal methods
Prog. Aerosp. Sci., vol. 80, pp. 18–32, 2016.

[7] C. Bonnal, J. M. Ruault, and M. C. Desjean
Active debris removal: recent progress and current trends
Acta Astronaut., vol. 85, pp. 51–60, 2013.

[8] W. K. Yoon *et al.*
Model-based space robot teleoperation of ETS-VII manipulator
IEEE Trans. Robot. Autom., vol. 20, no. 3, pp. 602–612, Jun. 2004.

[9] B. Bischof *et al.*
ROGER- Robotic geostationary orbit restorer
Sci. Technol. Ser., vol. 109, pp. 183–193, 2004.

[10] T. R. Kane and D. A. Levinson
Deployment of a cable-supported payload from an orbiting spacecraft
J. Spacecr. Rockets, vol. 14, no. 7, pp. 409–413, 1977.

[11] V. V. Beletsky and E. M. Levin
Dynamics of space tether systems
In *Advances in the Astronautical Sciences*. San Diego, CA, USA, Amer. Astronaut. Soc., 1993.

[12] K. K. Mankala and S. K. Agrawal
Dynamic modeling of satellite tether systems using Newton's laws and Hamilton's principle
J. Vib. Acoust.-Trans. ASME, vol. 130, no. 1, pp. 1–6, 2008.

[13] M. Krupa
Modelling, dynamics and control of tethered satellite systems
Nonlinear Dyn., vol. 43, no. 1, pp. 73–96, 2006.

[14] A. K. Misra
Dynamics and control of tethered satellite systems
Acta Astronaut., vol. 63, no. 11, pp. 1169–1177, 2008.

[15] P. Williams
Deployment/retrieval optimization for flexible tethered satellite systems
Nonlinear Dyn., vol. 52, no. 1, pp. 159–179, 2008.

[16] H. A. Fujii *et al.*
Dynamics of a flexible space tether equipped with a crawler mass
J. Guid. Control Dyn., vol. 31, no. 2, pp. 436–440, 2008.

[17] V. S. Aslanov *et al.*
Dynamics of space elevator after tether rupture
J. Guid. Control Dyn., vol. 36, no. 4, pp. 986–992, 2013.

[18] J. L. Tang *et al.*
Dynamics of variable-length tethers with application to tethered satellite deployment
Commun. Nonlinear Sci. Numer. Simul., vol. 16, no. 8, pp. 3411–3424, 2011.

[19] K. D. Kumar
Review of dynamics and control of nonelectrodynamic tethered satellite systems
J. Spacecr. Rockets, vol. 43, no. 4, pp. 705–20, 2006.

[20] M. P. Cartmell and D. J. McKenzie
A review of space tether research
Prog. Aerosp. Sci., vol. 44, no. 1, pp. 1–21, 2008.

[21] K. K. Mankala and S. K. Agrawal
Dynamic modeling and simulation of impact in tether net/gripper systems
Multibody Syst. Dyn., vol. 11, no. 3, pp. 235–250, 2004.

[22] J. F. Liu *et al.*
Dynamics of short tether-net system during deorbiting
Aircr. Eng. Aerosp. Technol., vol. 87, pp. 284–291, 2015.

[23] G. Zhai *et al.*
On-orbit capture with flexible tether–net system
Acta Astronaut., vol. 65, no. 5, pp. 613–623, 2009.

[24] G. Zhai, J. Zhang, and Z. Yao
Circular orbit target capture using space tether-net system
Math. Probl. Eng., vol. 2013, 2013, Art. no. 601482.

[25] M. Gärdsback and G. Tibert
Deployment control of spinning space webs
J. Guid., Control, Dyn., vol. 32, no. 1, pp. 40–50, 2009.

[26] M. Gärdsback and G. Tibert
Optimal deployment control of spinning space webs and membranes
J. Guid., Control, Dyn., vol. 32, no. 5, pp. 1519–1530, 2009.

[27] H. T. Liu *et al.*
Dynamics of tether-tugging reorbiting with net capture
Sci. China Technol. Sci., vol. 57, no. 12, pp. 2407–2417, 2014.

[28] F. Zhang and P. F. Huang
Releasing dynamics and stability control of maneuverable tethered space net
IEEE/ASME Trans. Mechatron., vol. 22, no. 2, pp. 983–993, Apr. 2017.

[29] P. F. Huang *et al.*
Dynamics and configuration control of the maneuvering-net space robot system
Adv. Space Res., vol. 55, pp. 1004–1014, 2015.

[30] B. Buckham, M. Nahon, and G. Cote
Validation of a finite element model for slack ROV tethers
In *Proc. OCEANS 2000 MTS/IEEE Conf. Exhib.*, vol. 2, 2000, pp. 1129–1136.

[31] H. Schaub and I. I. Hussein
Stability and reconfiguration analysis of a circularly spinning two-craft coulomb tether
IEEE Trans. Aerosp. Electron. Syst., vol. 46, no. 4, pp. 1675–1685, Oct. 2010.

[32] I. Chang, S. Y. Park, and K. H. Choi
Nonlinear attitude control of a tether-connected multi-satellite in three-dimensional space
IEEE Trans. Aerosp. Electron. Syst., vol. 46, no. 4, pp. 1950–1968, Oct. 2010.

[33] M. Förg, F. Pfeiffer, and H. Ulbrich
Simulation of unilateral constrained systems with many bodies
Multibody Syst. Dyn., vol. 14, no. 2, pp. 137–154, 2005.

[34] P. F. Huang, Z. H. Hu, and F. Zhang
Dynamic modelling and coordinated controller designing for the manoeuvrable tether-net space robot system
Multibody Syst. Dyn., vol. 36, no. 2, pp. 115–141, 2016.

[35] A. Klarbring
Mathematical programming in contact problems
in M. H. Aliabadi, Ed. *Computational Methods for Contact Problems*. Amsterdam, The Netherlands: Elsevier, 1994.

[36] T. F. Coleman and Y. Li
On the convergence of interior-reflective newton methods for nonlinear minimization subject to bounds
Math. Program., vol. 67, nos. 1–3, pp. 189–224, 1993.

[37] J. I. Tahara *et al.*
An adaptive VSS control method with integral type switching gain
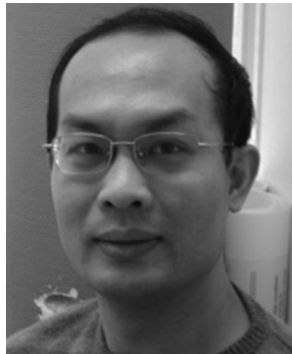*Proc. IASTED Int. Conf. Robot. Appl.*, 2001, pp. 106–111.

Zhongjie Meng (M'14) received the Ph.D. degree in aerospace science and technology from the Northwestern Polytechnical University, Xi'an, China, in 2010.

He is currently an Associate Professor in the School of Astronautics, Northwestern Polytechnical University. His research interests include dynamics and control of tethered space robots and intelligent spacecraft system.

Panfeng Huang (M'06) received the B.S. and M.S. degrees in control science and engineering from the Northwestern Polytechnical University, Xi'an, China, in 1998 and 2001, respectively, and the Ph.D. degree from the Chinese University of Hong Kong, Hong Kong, in the area of automation and robotics in 2005.

He is currently a Professor in the School of Astronautics and the Vice Director of the Research Center for Intelligent Robotics, Northwestern Polytechnical University. His research interests include tethered space robotics, intelligent control, machine vision, and space teleoperation.

Jian Guo received B.S. and M.S. degree from Northwestern Polytechnical University in the area of aircraft design in 1998, 2001, respectively, and Ph.D. from the University of Leeds in the area of mechanical engineering in 2010.

He is currently an Assistant Professor in the Faculty of Aerospace Engineering, Delft University of Technology, Delft, The Netherlands. His research interests include spacecraft systems engineering, multidisciplinary design optimization and its applications on space systems, spacecraft formation flying, etc.